Ex-situ n-type heavy doping of $Ge_{1-x}Sn_x$ epilayers by surface Sb deposition and pulsed laser melting

Daris Fontana[1,*], Francesco Sgarbossa[1,2,*,‡], Ruggero Milazzo[1], Enrico Di Russo[1,2,3], Emmanuele Galluccio[4], Davide De Salvador[1,2], Ray Duffy[4], and Enrico Napolitani[1,2,5].

1) Università degli Studi di Padova, Dipartimento di Fisica e Astronomia, via Marzolo 8, 35131 Padova, Italia.

2) Istituto Nazionale di Fisica Nucleare, Laboratori Nazionali di Legnaro, viale dell'Università 2, 35020 Legnaro (PD), Italia.

3) CNR-IMM, Via Gobetti 101, Bologna, 40129, Italy.

4) Tyndall National Institute, University College Cork, Lee Maltings, Cork T12 R5CP, Ireland.

5) CNR-IMM, Via S. Sofia 64, 95123 Catania, Italy.

(*) These authors contributed equally to this work.

(‡) Corresponding author.

Abstract

$Ge_{1-x}Sn_x$ alloys have attracted considerable attention for their promising electrical and optical properties. One of the main challenges for their successful implementation in devices concerns the fabrication of n-type heavily doped surface layers. In this work, a new methodology for ex-situ doping of $Ge_{1-x}Sn_x$ layers is investigated. It consists in the deposition of Sb atoms on the surface of $Ge_{1-x}Sn_x$ layers followed by pulsed laser melting (PLM) that ensures the diffusion of Sb into the alloy. We demonstrate that Sb is incorporated very efficiently within a relaxed $Ge_{0.91}Sn_{0.09}$ epilayer, with supersaturated 4×10^{20} cm^{-3} active concentrations, in line with literature records obtained in $Ge_{1-x}Sn_x$ with in-situ approaches. At the same time, we evidence that the concentration of substitutional Sn close to the surface decreases from 9 to about 6 at. % after PLM, inducing a contraction of the lattice parameter perpendicular to the underlying $Ge_{1-x}Sn_x$. These results demonstrate a possible route for ex-situ n-type heavy doping of $Ge_{1-x}Sn_x$ alloys, but indicate also that Sn redistribution and precipitation phenomena need to be carefully considered for a successful process development.

Keywords

Pulsed laser melting, laser processing, doping, antimony, GeSn, Ge.

Introduction

In the last decade $Ge_{1-x}Sn_x$ alloys have received considerable attention for future mid-infrared photonics, radiation detectors and nanoelectronics [1–6]. For the above mentioned applications, high quality $Ge_{1-x}Sn_x$ can be fabricated with several grown technologies, including molecular beam epitaxy (MBE), physical vapor deposition (PVD) and chemical vapor deposition (CVD) [4,5]. In particular, the integration of

GeSn alloys in devices like photodetectors and lasers requires not only high Sn concentrations, but also high doping levels [3]. However, the simultaneous integration of Sn and high doping levels in Ge remains a challenge, especially for n-type doping [3]. The use of in-situ doping technologies is an attractive route to obtain materials with high doping activation levels. Considerable efforts were then made to optimize low temperature growth processes, as Sn precipitation or out-diffusion are prone to occur at relatively high temperatures (> 400 °C) [7]. On the other hand, ex-situ techniques are an effective alternative, thanks to their ability to achieve doped layers with the high spatial control required for device development. Furthermore, they give an extra degree of freedom (or an option) for tunability of these materials. Ion implantation has long been the industry leading method to achieve depth and laterally controlled doping profiles. Nonetheless, this approach requires a post-implantation annealing to recover the crystal damage. In order to do this, rapid thermal annealing (RTA) or flash-lamp annealing (FLA) [8] non-equilibrium thermal processes are the preferred solution. In particular, the fast temperature increase of the sample surface during FLA leads to sample recrystallization in the milli-second range, reducing Sn redistribution. In the last years, Pulsed Laser Melting (PLM) also emerged as a promising technique to overcome the limitations of traditional rapid processes (e.g., Sn segregation, cellular breakdown) and achieve better material performances [9]. The use of ultra-violet (UV) laser pulses with duration in the nano-second time scale has the substantial advantage of confining the thermal treatment in close proximity of the irradiated area. In addition, high-energy laser pulses can melt the topmost layers of Ge-based alloys, leading to ultra-fast recrystallization associated with a remarkable increase of the solid phase solubility of most of foreign atoms, including Sn [10].

Recently, PLM was successfully adopted to fabricate highly n-doped layers in the near-surface of Ge substrate [11]. The innovative approach proposed consisted in depositing a thin film of Sb on top of Ge [12], and then making it to diffuse in the laser-induced molten phase. Then, the ultra-fast material re-crystallization leads to the formation of high quality Ge:Sb alloys with record active concentration and ultralow resistivity, demonstrating PLM as a promising route for ex-situ Ge hyperdoping[11] [13]. In this paper, we demonstrate that a similar method can be successfully applied to heavily dope a high Sn-content $Ge_{1-x}Sn_x$ alloy by Sb deposition followed by PLM. As we will show, record Sb active concentrations are reached, but Sn redistribution and precipitation need to be carefully evaluated.

Experimental

Sample preparation

$Ge_{1-x}Sn_x$:Sb films were fabricated by processing commercial substrates supplied by IQE. These consists in an un-doped epilayer of $Ge_{1-x}Sn_x$ (thickness 1.2 μm) grown on a virtual Ge buffer layer (700nm), over a <001> Si substrate. Two substrates with similar Sn concentrations were used, namely 8.4 at. % ($Ge_{0.916}Sn_{0.084}$), or 9.4 at. % ($Ge_{0.906}Sn_{0.094}$), as determined by Rutherford Backscattering Spectrometry (RBS). As it will be shown in the following, the two substrates gave very similar results. Then, a 2 nm thick Sb layer was deposited on the top of $Ge_{1-x}Sn_x$ by DC sputtering at room temperature using a high purity (99.999 %) Sb target supplied by ACI Alloys. In order to reduce all contaminations, the sputtering chamber was evacuated at pressure below 10^{-4} Pa before any deposition[12]. A Si control substrate was also placed in the chamber during the deposition to accurately evaluate the Sb areal density by RBS, which resulted to be 9 x 10^{15} at/cm². Lastly, PLM was performed to diffuse the Sb atoms into the $Ge_{1-x}Sn_x$ layers, using a

Coherent COMPex 201F KrF excimer laser emitting light with λ = 248 nm, 22 ns pulse duration, over a 5 × 5 mm^2 square spot with 2% uniformity ad 0.7% reproducibility. Single pulses were shot with energy density ranging from 400 to 700 mJ/cm^2. An exhaustive list of the specimens analyzed in this study is presented in Table 1.

Characterization techniques

Rutherford Backscattering Spectrometry (RBS) was performed using a 2.0 MeV ^{4}He$^+$ beam (scattering angle: 160°) at the AN2000 and CN Van de Graaff accelerators located at the *Laboratori Nazionali di Legnaro* (LNL-INFN). Random spectra (random-RBS) were obtained by rotating random procedures performed using a high-resolution goniometer (angular resolution: 0.01°). Channeling measurements (c-RBS) were performed by aligning the beam with the <001> or <111> sample axis (axial channeling) [14]. Random-RBS and c-RBS data were used to estimate, in a topmost layer 50 nm thick, the concentrations of Sn and of substitutional Sn respectively, as described in ref. [15]. As the Sn and Sb atomic masses are too close together to be distinguished by the technique, in samples doped with Sb the extracted values correspond to the concentration of the sum of Sn and Sb atoms.

Secondary Ion Mass Spectrometry (SIMS) depth profiles were acquired using a CAMECA IMS-4f spectrometer with a 5.5 keV Cs$^+$ ion beam rastered over a 250 × 250 μm^2 area, while collecting ^{133}Cs^{121}Sb$^+$ and ^{133}Cs^{119}Sn$^+$ ions, according to the CsM$^+$ measurement protocol to minimize matrix effects [16]. The depth scales were calibrated by measuring each SIMS crater with a KLA-Tencor P-17 profilometer. The Sn concentration was calibrated by estimating the Sn Relative Sensitivity Factor (RSF) in the pristine GeSn samples assuming the Sn fraction provided by RBS. The Sb concentration was calibrated by measuring a standard with known Sb areal density in a Ge matrix and assuming the same RSF in the GeSn matrix. Data that will be shown in the following suggest that the procedure adopted for the Sb calibration is accurate in agreement with ref [16]. The overall error of the Sb concentration is ±10 % (relative error) and of the Sn concentration is ±0.1 at. %.

High-Resolution X-ray Diffraction (HR-XRD) reciprocal lattice maps were recorded for both symmetric (004) and asymmetric (224) reflections, by using a Panalytical MRD X'Pert Pro diffractometer equipped with a Cu anode source, a multilayer W/Si parabolic mirror and a Bartels 4 bounce Ge (220) monochromator. In particular, the Kα_1 radiation (8 keV) was selected as the probe and the angular acceptance was reduced to 12 arcsec by a channel-cut (220) analyzer equipped detector.

Electrical properties were analyzed according to the Van der Pauw-Hall method using a four-point probe apparatus supplied by MMR Technologies. This consists in four gold probes arranged in a square geometry and placed at the corners of each sample. These are connected to a Keithley source-meter and a switch matrix in order to sequentially perform measurements of the sheet resistance R$_s$ and of the Hall coefficient RHs [13,17]. From the RHs and R$_s$ values the carrier Hall dose N$_s$ and carrier Hall mobility μ$_s$ are also easily calculated [17]. In our case, thanks to the chemical Sb concentration depth profiles provided by the SIMS analyses, we also estimated the maximum Sb active concentration n$_{max}$, with an error of ±10%, using the following procedure. Starting from the SIMS profile, we calculated n$_{max}$ such that the dopant concentration where SIMS profile integrals correspond to the Hall carrier dose (assuming the Hall scattering factor equal to 1). Examples resulting from this procedure are reported in the supplementary information.

Results and Discussion

Table 1. Composition, structural and electrical parameters determined for the samples before and after PLM. Notes: Maximum Sb active concentration is calculated from Hall (see additional information) and SIMS data as described in the text. RBS data are relative to the concentrations in a topmost layer 50 nm thick and, in the first three samples (i.e. the sample without Sb) data are referred to the only Sn. In samples after PLM, HRXRD data are calculated from the secondary $Ge_{1-x}Sn_x$ peak. The Sn substitutional concentration was calculated by subtracting the active Sb concentration from the substitutional (Sn+Sb) concentration measured by c-RBS.

Sample	Laser energy density (mJ/cm^2)	Maximum Sb conc. (10^{20} cm^{-3})	Maximum Sb active conc. (10^{20} cm^{-3})	RBS (Sn+Sb) conc. (at. %)	c-RBS (Sn+Sb) substitutional conc. (at. %)	Sn substitutional conc. (at. %)	HRXRD Misfit w.r.t. Ge$_{rel}$ (%)	HRXRD Parallel strain (%)	HRXRD Sn conc. (at. %)
Ge$_{0.916}$Sn$_{0.084}$	-	-	-	8.4 ± 0.2	8.2 ± 0.2	8.2 ± 0.2	1.20 ± 0.06	-0.08 ± 0.02	8.2 ± 0.4
Ge$_{0.906}$Sn$_{0.094}$	-	-	-	9.4 ± 0.2	9.2 ± 0.2	9.2 ± 0.2	1.25 ± 0.06	-0.12 ± 0.02	8.5 ± 0.4
Ge$_{0.906}$Sn$_{0.094}$	500	-	-	9.4 ± 0.2	6.1 ± 0.2	6.1 ± 0.2	0.94 ± 0.05	0.19 ± 0.02	6.4 ± 0.3
Ge$_{0.916}$Sn$_{0.084}$:Sb	400	12.6 (2.9 at.%)	4.0 (0.9 at.%)	10.8 ± 0.2	7.0 ± 0.2	6.1 ± 0.3	-	-	-
Ge$_{0.916}$Sn$_{0.084}$:Sb	500	10.4 (2.4 at.%)	3.1 (0.7 at.%)	10.5 ± 0.2	6.8 ± 0.2	6.1 ± 0.3	0.88 ± 0.04	0.24 ± 0.02	6.0 ± 0.2
Ge$_{0.916}$Sn$_{0.084}$:Sb	600	7.7 (1.8 at.%)	2.6 (0.6 at.%)	10.6 ± 0.2	6.7 ± 0.2	6.1 ± 0.2	-	-	-
Ge$_{0.906}$Sn$_{0.094}$:Sb	700	8.0 (1.8 at.%)	4.1 (0.9 at.%)	11.0 ± 0.2	6.9 ± 0.2	6.0 ± 0.2	0.84 ± 0.04	0.29 ± 0.02	5.7 ± 0.2

The samples studied in this work are detailed in Table 1. The compositional, structural and electrical characterizations of Ge$_{1-x}$Sn$_x$:Sb layers were carried out on 4 samples after PLM with energy density ranging from 400 to 700 mJ/cm^2. These samples were compared with the two pristine Ge$_{1-x}$Sn$_x$ samples (x = 8.4 and 9.4 at. %), and with a Ge$_{1-x}$Sn$_x$ sample processed at 500 mJ/cm^2 without any previous Sb deposition.
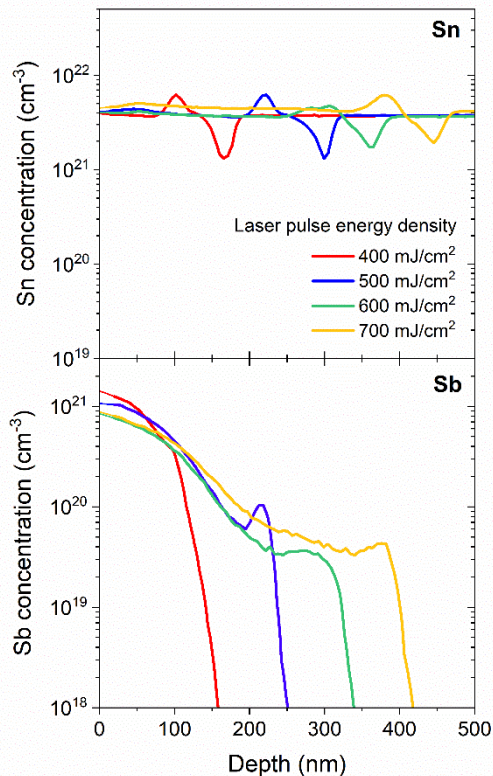
Figure 1. SIMS data of Ge$_{1-x}$Sn$_x$:Sb samples after PLM at different energy densities. Sn (top panel) and Sb (bottom panel) chemical profiles are represented with the same depth scale. □The profiles were extrapolated to the surface within the first 10–20 nm (thin lines), where SIMS exhibit significant artifacts.

The Sn and Sb concentration profiles of Ge$_{1-x}$Sn$_x$:Sb layers are plotted in Fig. 1. It is straightforward to observe that Sb has diffused into Ge$_{1-x}$Sn$_x$ following PLM, reaching extremely high top-concentrations up to ~1 x 10^{21} cm^{-3}. In particular, Sb has diffused from the surface into the laser-induced molten phase down to the maximum melt depth (MMD) in correspondence of which a diffusivity drop occurs [10]. This leads to the formation of a highly-doped Ge$_{1-x}$Sn$_x$:Sb layer in correspondence of the sample surface, followed by a pronounced negative gradient of Sb concentration and then a sharp concentration drop in correspondence of the MMD (see Fig. 1). It should be noted that the MMD increases from ~150 to ~400 nm with the increase of the pulse energy density from 400 to 700 mJ/cm^2, consistently with the higher energy released within the material and available for melting. On the other hand, an increase of the MMD leads also to a redistribution of the Sb over greater depths, decreasing the maximum Sb concentration from 1.3 to 0.8 × 10^{21} cm^{-3}, as reported in Table 1. Consistently, the areal densities of the diffused Sb calculated from SIMS profiles are constant within the ±10 % error varying the PLM energy density, and these values are also compatible with the deposited Sb areal density measured by RBS. This suggests that all the deposited Sb atoms readily diffuse within the Ge$_{1-x}$Sn$_x$ liquid phase during PLM with neither out-diffusion nor surface segregation. Furthermore, the absence of any variation in the Sb areal density supports the accuracy of the Sb SIMS calibration procedure.

Interestingly, an Sb concentration peak is also observed just before the MMD. This is similar to the well-known pile-up anomalous diffusion phenomena already observed to occur close to the liquid-solid interface for many impurities during PLM in Si and Ge [10][18][19], suggesting that such kind of phenomena occur also in $Ge_{1-x}Sn_x$. Furthermore, a comparison with a previous study done in similar conditions in a pure Ge matrix [11], reveals that deeper junctions are formed in $Ge_{1-x}Sn_x$. For example, after 1 pulse at 500 mJ/cm^2 a Sb concentration equal to 1 x 10^{18} cm^{-3} is reached in $Ge_{1-x}Sn_x$ and Ge substrates at the depths of 160 nm (Fig. 1, present work) and 120 nm (Fig. 1, ref [11]), respectively. This is explained in terms of the lower melting temperature of $Ge_{1-x}Sn_x$ compared to Ge [20]. Furthermore, despite the Sn composition was very uniform in pristine $Ge_{1-x}Sn_x$ epilayers (data not shown here), after PLM a pronounced redistribution of Sn atoms is observed in Fig. 1 approaching the MMD, with a Sn pile-up followed by a dip. Presumably, this redistribution is related with the same anomalous diffusion behavior discussed above for Sb.
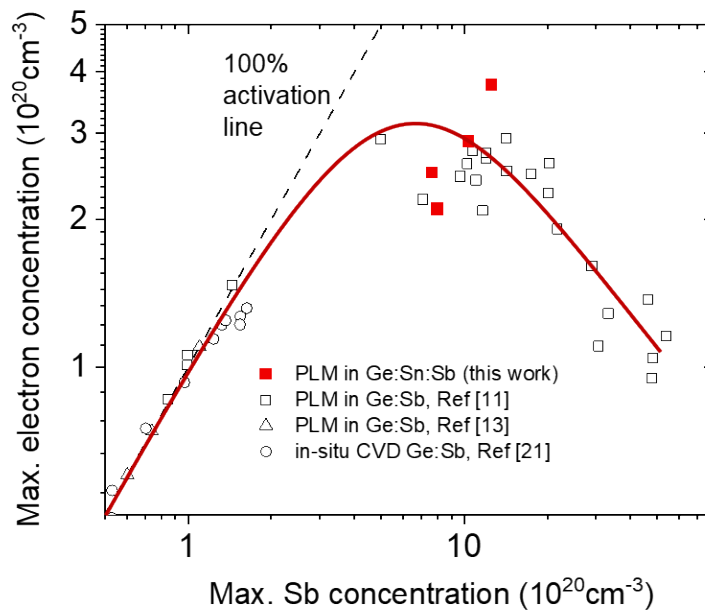

Figure 2. Maximum active electron concentrations vs. maximum Sb chemical concentration in $Ge_{1-x}Sn_x$ (red filled squares), compared with literature data obtained in Ge:Sb (open symbols). The black dashed line indicates the full electrical activation of Sb. The red line is a guideline of the experimental data.

Table 1 reports the maximum Sb electrical active concentrations extracted by VdP-Hall (see the experimental section and the supplementary material for more details). These values are also reported in Fig. 2 as a function of the corresponding maximum Sb chemical concentrations, and also compared with other results provided in literature concerning active Sb in a Ge matrix [11][13][21]. Our data shows that the electrical active concentrations of Sb are about a factor of 3 lower than the corresponding maximum chemical concentrations, indicating a partial electrical activation of dopant atoms. However, the obtained concentrations are remarkably high, in the range 2 to 4 × 10^{20} cm^{-3}. These activation levels are comparable with the highest value reported so far for n-type doping in $Ge_{1-x}Sn_x$ [3], that is 5 x 10^{20} cm^{-3}, obtained by in-situ Sb doping of a 200nm $Ge_{0.93}Sn_{0.07}$ layer by Zheng and co-workers [22]. This demonstrates that n-type heavy doping of $Ge_{1-x}Sn_x$ can be successfully performed also by an ex-situ approach if PLM is properly exploited. It is interesting to note that our data are compatible with the trend depicted in Fig. 2, and in

addition they are placed at the top of the activation curve. Therefore, the $Ge_{1-x}Sn_x$ matrix seems to allow the same high Sb activation values observed in Ge, more than one order of magnitude higher than the equilibrium Sb solid solubility limit in Ge [23].
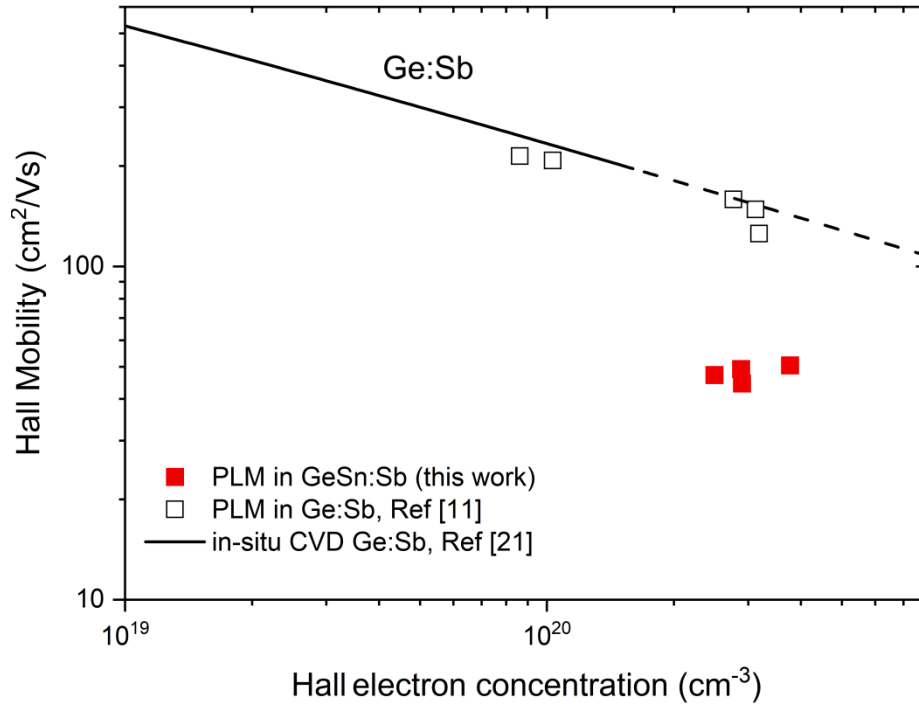

Figure 3. Electron Hall mobility vs. maximum electron concentration in $Ge_{1-x}Sn_x$:Sb (red filled squares), compared with literature data obtained in Ge:Sb [11,21] (open squares and black line).

The carrier Hall mobilities measured by VdP-Hall are reported as a function of the Hall maximum carrier concentration (filled red squares) in Fig 3. Results are also compared with other literature data concerning Ge doped with Sb by PLM (open square symbols) [11] and with the trend set out by fully active Sb in Ge grown by in-situ CVD (black line) [21]. The mobility of the $Ge_{1-x}Sn_x$:Sb layers appear lower than the mobility values reported for Ge:Sb. This is quite surprising, as the electron mobility in $Ge_{1-x}Sn_x$ is indeed expected to be higher than in Ge [3]. We cannot exclude that this effect is partially due to an enhanced carrier scattering due to not active Sb atoms. However, it is worth noting that in the Ge matrix the inactive Sb after PLM seem to have no significant role in the electron mobility. This is strongly suggested by Ge:Sb data reported by Carraro et al. [11], which have similar partial activation as our data and nicely extrapolate the trend for fully active Sb in Ge. The data that will be shown hereafter will provide further possible explanations.
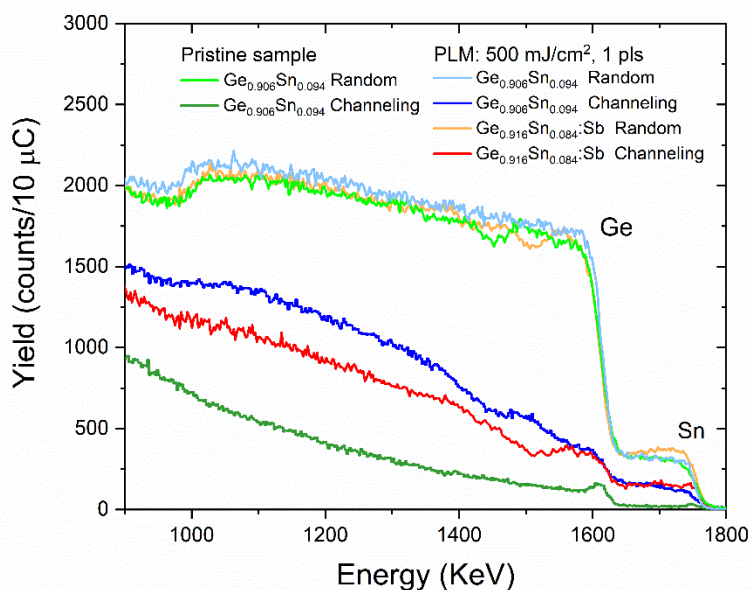
Figure 4. Rutherford Backscattering random and [001] axial channeled spectra acquired using a 2.0 MeV He$^+$ beam. Ge and Sn regions are shown.

To get insights on the composition and the crystal quality of the samples, we performed detailed RBS and c-RBS characterization. Fig. 4 reports selected spectra in pristine sample, and in samples after PLM at 500mJ/cm^2 both with and without Sb, recorded both in random and channeling conditions. From the spectra we extracted Sn+Sb concentrations (we remind that the technique cannot distinguish between Sb and Sn in $Ge_{1-x}Sn_x$:Sb samples) and the corresponding substitutional concentrations, as reported in Table 1. Random spectra are quite similar each other, except for a slightly larger signal in the sample with Sb due to the additional Sb Yield superimposed to the Sn Yield. Consistently, the extracted Sn+Sb concentrations of the $Ge_{1-x}Sn_x$:Sb samples reported in Table 1 are larger than in the samples without Sb.

C-RBS spectrum of the pristine sample shows a low yield, indicating a very good Sn substitutionality. Correspondingly, the substitutional concentrations reported in Table 1 for pristine samples are compatible with the total ones, indicating that almost all Sn atoms, within errors, are in substitutional positions and bonded with Ge atoms[24]. It must be noted that Sn-Sn pairs would induce deviations of the Sn atoms from the exact substitutional positions and, if present at not negligible concentration, they would induce an increase of the c-RBS yield. These values are in line with the literature [25] [26] and confirm an high starting material quality.

After PLM, channeling spectra show instead a different behavior, with intermediate yields between the c-RBS pristine sample and the random spectra. This indicates a reduction of substitutional concentration as a result of the PLM processes. The substitutional concentrations reported in Table 1 after PLM are always lower (by about 30-40 %) than the corresponding total concentrations, with a 6.1 at. % value for the sample without Sb, and higher values, in the range 6.7-7.0 at. %, in the samples with Sb. It must be noted that in the latter samples part of the substitutional concentration is due to substitutional, electrically active, Sb atoms. Here, an estimate of the substitutional Sn concentration can be done by

subtracting the maximum Sb active concentration measured by VdP-Hall to the Sn+Sb substitutional concentration, as reported in Table 1. It is interesting to note that, after this correction, all the substitutional Sn concentrations results compatible with 6.1 at. %, both with and without Sb, within the experimental error. This indicates that PLM limits the Sn substitutional concentration to about 6.1 at. %, independently on the presence of Sb and on slight variations of the pristine Sn concentration, and with no significant dependence on the laser energy density and on the maximum melt depth. In other words, during PLM the Sb and Sn atoms seem to incorporate in the lattice independently of each other. Still, the above Sn substitutional concentrations are higher than the Sn equilibrium solid solubility in Ge (<1% [3,27]), and in line with the best results reported in literature on Sn incorporation in Ge during PLM [9] [28]. Therefore the above 6 at.% might represent a limit for Sn incorporation in Ge by PLM. However, we cannot exclude that in the above phenomenon a role is also played by the extended defects which are present in the samples prior to PLM (as evidenced by HRXRD measurements discussed below) mostly located deeper than RBS sensitivity (beyond 50nm). Furthermore, the above results could provide a further explanation for the reduced electron mobility reported in Fig. 3, as the observed appreciable amount of Sn atoms in displaced lattice sites might enhance the carrier scattering.

To investigate the lattice modification induced by PLM we performed HRXRD reciprocal space mapping (RSM) around symmetrical (004) and asymmetrical (224) reflections. In particular, (224) RSM of selected samples are reported in Fig. 5 before (left panels) and after PLM (right panels). Data are reported both without Sb (panels a) and b)), and with Sb (panels c) to f)). The respective (004) RSM of the as-grown samples are reported in the supplementary material. To make it easier to read the maps, the origin (0;0) of the reciprocal space is translated at the unstrained bulk Si substrate reciprocal lattice point (RLP) maximum ($Q_{//}^{Si}$; $Q_{\perp}^{Si}$), not shown in Fig. 5. Samples before PLM (panels a), c), and e)) exhibit two peaks: one is related to the Ge buffer, the second one to the $Ge_{1-x}Sn_x$ layer, appearing in the upper and bottom part of the RSM, respectively. The peak ascribed to the Ge buffer is located to the left of the black dashed [224] line (i.e., the line corresponding to perfect cubic cell), indicating the presence of a small tensile strain. This strain is induced by the different thermal expansion coefficient between Ge and Si and it develops during the cool-down from the growth temperature, where almost full strain relaxation takes place [29, 30, 31]. On the contrary, the $Ge_{1-x}Sn_x$ peak appears to the right side of the [224] line. Therefore, the $Ge_{1-x}Sn_x$ is not fully relaxed, with a small residual compressive strain, despite a thermal expansion coefficient even larger than Ge [32]. Further information concerning the crystalline quality of the various layers were extracted by examining their diffracted intensity distributions. Ge buffers show a narrow, circular-shaped peaks, suggesting a relatively low number of extended defects [33], such as misfit dislocations [34], which presumably are confined close to the Si substrate. On the other hand, a $Ge_{1-x}Sn_x$ peak broadening orthogonally to the direction [224] is clearly visible in RSMs (224) reflections. This suggests the presence of a network of misfit dislocations distributed within the film, responsible for the observed (partial) strain relaxation, and leading to a distribution of cells with a slightly different degree of relaxation.
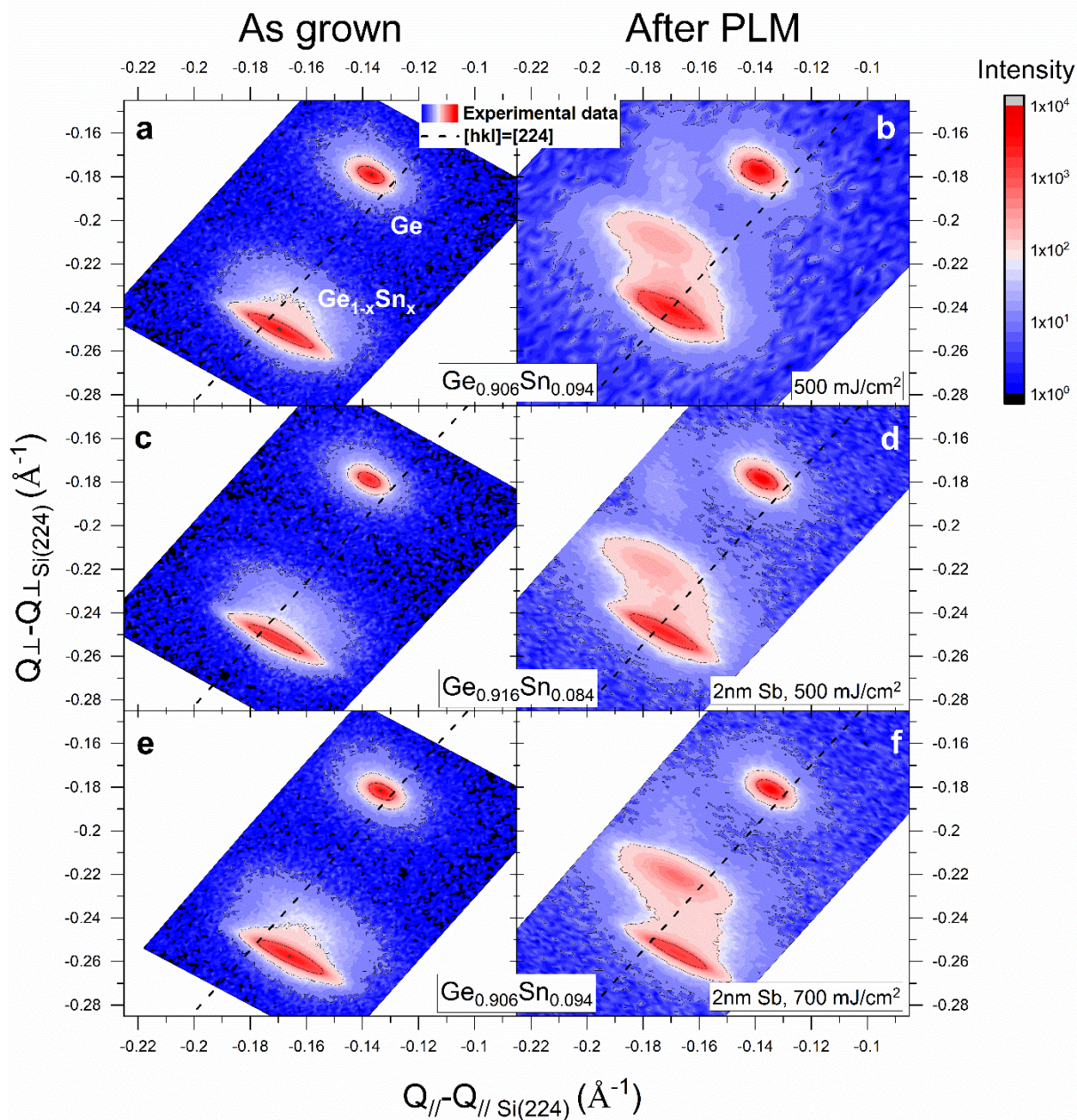
Figure 5. HRXRD reciprocal space maps in the (224) reflection region: (a) pristine $Ge_{1-x}Sn_x$ (x = 9.4 %); (b) same sample processed at 500 mJ/cm^2; (c) pristine $Ge_{1-x}Sn_x$ (x = 9.4%); (d) same sample after 2 nm Sb deposition and laser processing at 500 mJ/cm^2; (e) pristine $Ge_{1-x}Sn_x$ (x = 9.4%); (f) same sample after 2 nm Sb deposition and laser processing at 700 mJ/cm^2. The black dashed line is the reference for the [224] direction in the reciprocal space.

In order to extract quantitative parameters, we calculated the misfit (change of lattice parameter due to Sn alloying) and the parallel strain (with respect to the relaxed substrate) of the $Ge_{1-x}Sn_x$ layer from the positions of the $Ge_{1-x}Sn_x$ RSM peaks by following the same procedure adopted in ref [35] [36] [37]. Specifically, we estimated the Sn concentration, reported in Table 1, from misfit values by assuming the Vegard's law [38]. Consistently with the qualitative observations made above, a small compressive strain of about -0.1% is present in both the as grown samples. Furthermore, the Sn concentrations estimated by HRXRD are, consistently, in good agreement with the (substitutional) Sn concentration estimated by RBS.

After PLM (Figures 5, panels b), d), f)), a secondary $Ge_{1-x}Sn_x$ peak appears in all the samples, with a $Q_{//}$ almost identical to the main $Ge_{1-x}Sn_x$ peak but with a higher $Q_\perp$. At the same time most of the other RSMs features remain unchanged, i.e. the Ge buffer peak and the main $Ge_{1-x}Sn_x$ peak remain almost at the same positions as the Ge and $Ge_{1-x}Sn_x$ peaks observed before the processes (Fig. 5, panels a), c), e)). These results suggest that the surface layer subjected to PLM, i.e. the region down to the maximum melt depth (see Fig. 1), changes its lattice parameters, whereas the remaining of the 1200 nm thick $Ge_{1-x}Sn_x$ layer and the Ge buffer remain unchanged. This confirms the local nature of the PLM thermal processes and their ability to induce material modifications with a high depth control. According to the observed change in the Q values, which goes as the reciprocal of lattice parameter, the surface layer undergoes a lattice contraction, with a perpendicular lattice parameter smaller than the underlying $Ge_{1-x}Sn_x$, whereas the parallel lattice parameter remains unchanged. The origin of the lattice contraction can be easily attributed to the reduction of substitutional Sn discussed previously (see Fig. 4 and Table 1). At the same time, the fact that the parallel lattice parameter remains unchanged indicates that the surface layer subjected to PLM remains pseudomorphic to the underlying $Ge_{1-x}Sn_x$ and, presumably, with no formation of additional misfit dislocations.

The same procedure described above was apply to the secondary peaks to extract the misfit and parallel strain values of the $Ge_{1-x}Sn_x$ surface layer was than applied to the secondary peaks. Results are reported in Table 1. Besides, it is worth noting that Sb heavy doping is confined within a layer that is much shallower that the maximum melt depths observed in Fig. 1. Therefore, the position of the secondary peaks in Fig. 5, and thus the averaged lattice parameter of the surface layers, receives small or negligible contribution from the Sb atoms. We therefore used the misfit values to calculate the Sn concentrations reported in Table 1, similarly to what done previously in pristine samples. These values are estimated by assuming the Vegard's law [38], by making the additional assumption that the non-substitutional Sn atoms induce negligible lattice modification and also, for the reason described above, neglecting any Sb contribution to the position of the $Ge_{1-x}Sn_x$ secondary peak. It is clear that, under these assumptions, the calculations values refer to the concentration of substitutional Sn, i.e. those atoms able to induce a lattice expansion, and not to the total ones.

Table 1 shows that the misfit changes from about 1.2 % in the pristine samples, to the range 0.84 to 0.94 % after PLM, with a reduction of about -0.3 %. Correspondingly, the parallel strain changes from compressive of about -0.1 % to tensile in the range 0.19 to 0.29 %., with an increase of about +0.3%, i.e. opposite to the misfit decrease, confirming the absence of any strain relaxation during the PLM processes. Concerning the Sn concentrations calculated from the misfit values and reported in Table 1, it is worth noting that these are in excellent agreement with the substitutional Sn concentrations estimated by the c-RBS and VdP-Hall data. This further confirms the consistency of our data, and supports the assumptions made, in particular that the non-substitutional Sn induce no significant lattice expansion.

Conclusion

In this work, we demonstrate that pulsed laser melting is effective to introduce ex-situ Sb atoms in $Ge_{1-x}Sn_x$ alloys, generating heavily-doped $Ge_{1-x}Sn_x$:Sb layers with active concentration up to 4×10^{20} cm^{-3}. The structural and chemical characterizations reveal minimal Sn redistributions. The PLM processes ensured a good epitaxial recrystallization of the matrix after the melting processes, even if a reduction of the Sn substitutional fraction down to about 6 at. % and moderate carrier mobilities were observed. The

above data suggest that the Sn concentration needs to be properly tuned for a successful Sb doping of $Ge_{1-x}Sn_x$ by PLM.

Abbreviations

PLM pulsed laser melting, VdP Van der Pauw, HRXRD High Resolution X-Ray Diffraction, RBS Rutherford backscattering spectrometry, c-RBS channeling Rutherford backscattering spectrometry, SIMS secondary ion mass spectrometry, PLM pulsed laser melting, RSM Reciprocal Space Map, RLP Reciprocal lattice point, CVD chemical vapor deposition, MMD maximum melt depth.

Declaration of Competing Interest

The authors declare that they have no known competing financial interests or personal relationships that could have appeared to influence the work reported in this paper.

Bibliography

1. Pillarisetty, R. Academic and industry research progress in germanium nanodevices. *Nature* **479**, 324–328 (2011).

2. Zhou, Z., Yin, B. & Michel, J. On-chip light sources for silicon photonics. *Light Sci. Appl.* **4**, 1–13 (2015).

3. Miao, Y. *et al.* Review of Si-based GeSn CVD growth and optoelectronic applications. *Nanomaterials* **11**, (2021).

4. Wirths, S., Buca, D. & Mantl, S. Si-Ge-Sn alloys: From growth to applications. *Prog. Cryst. Growth Charact. Mater.* **62**, 1–39 (2016).

5. Zaima, S. *et al.* Growth and applications of GeSn-related group-IV semiconductor materials. *Sci.*

Technol. Adv. Mater. **16**, 43502 (2015).

6. Senaratne, C. L. *et al.* Direct gap Ge1-ySny alloys: Fabrication and design of mid-IR photodiodes. *J. Appl. Phys.* **120**, (2016).

7. Aubin, J., Hartmann, J.-M., Barnes, J.-P., Pin, J.-B. & Bauer, M. Very Low Temperature Epitaxy of Heavily In-situ Phosphorous Doped Ge Layers and High Sn Content GeSn Layers. *ECS Trans.* **MA2016**-02, 2032–2032 (2016).

8. Oka, H. *et al.* Non-equilibrium solid-phase growth of amorphous GeSn layer on Ge-on-insulator wafer induced by flash lamp annealing. *Appl. Phys. Express* **14**, (2021).

9. Tran, T. T. *et al.* Synthesis of Ge1-xSnx alloys by ion implantation and pulsed laser melting: Towards a group IV direct bandgap material. *J. Appl. Phys.* **119**, (2016).

10. Fuccio, C. & La Magna, A. *Laser annealing process in semiconductor techology*. (Elsevier, 2021).

11. Carraro, C. *et al.* N-type heavy doping with ultralow resistivity in Ge by Sb deposition and pulsed laser melting. *Appl. Surf. Sci.* **509**, 145229 (2020).

12. Maggioni, G. *et al.* Diffusion doping of germanium by sputtered antimony sources. *Mater. Sci. Semicond. Process.* **75**, 118–123 (2018).

13. Sgarbossa, F. *et al.* Self-limiting Sb monolayer as a diffusion source for Ge doping. *Appl. Surf. Sci.* **496**, 8–9 (2019).

14. Bagli, E. *et al.* Enhancement of the Inelastic Nuclear Interaction Rate in Crystals via Antichanneling. *Phys. Rev. Lett.* **123**, 044801 (2019).

15. Tesmer, J. R. & Nastasi, M. *Handbook of modern ion beam materials analysis*. (Material Research Society, 1995).

16. Gao, Y. A new secondary ion mass spectrometry technique for III-V semiconductor compounds using the molecular ions CsM+. *J. Appl. Phys.* **64**, 3760–3762 (1988).

17. van der Pauw, L. J. A method of measuring the resistivity and Hall coefficient on lamellae of arbitrary shape. *Philips Tech. Rev.* **20**, 220–224 (1958).

18. Fisicaro, G. *et al.* Anomalous impurity segregation and local bonding fluctuation in l-Si. *Phys. Rev. Lett.* **110**, 1–5 (2013).

19. Impellizzeri, G. *et al.* B-doping in Ge by excimer laser annealing. *J. Appl. Phys.* **113**, (2013).

20. Kasper, E., Kittler, M., Oehme, M. & Arguirov, T. Germanium tin: silicon photonics toward the mid-infrared. *Photonics Res.* **1**, 69 (2013).

21. Xu, C., Senaratne, C. L., Sims, P., Kouvetakis, J. & Menéndez, J. Ultralow Resistivity Ge:Sb heterostructures on Si Using Hydride Epitaxy of Deuterated Stibine and Trigermane. *ACS Appl. Mater. Interfaces* **8**, 23810–23819 (2016).

22. Zheng, J. *et al.* Fabrication of low-resistance Ni ohmic contacts on n+Ge1-xSnx. *IEEE Trans. Electron Devices* **65**, 4971–4974 (2018).

23. Olesinski, B. R. W., Abbaschian, G. J. & Diagram, E. The Ge-Sb (Germanium-Antimony) System. *Bull. Alloy Phase Diagrams* **7**, 219–222 (1986).

24. Gencarelli, F. *et al.* Extended X-ray absorption fine structure investigation of Sn local environment in strained and relaxed epitaxial Ge1-xSnx films. *J. Appl. Phys.* **117**, (2015).

25. Oehme, M. *et al.* Epitaxial growth of highly compressively strained GeSn alloys up to 12.5% Sn. *J. Cryst. Growth* **384**, 71–76 (2013).

26. Bhargava, N., Coppinger, M., Prakash Gupta, J., Wielunski, L. & Kolodzey, J. Lattice constant and substitutional composition of GeSn alloys grown by molecular beam epitaxy. *Appl. Phys. Lett.* **103**, 2–6 (2013).

27. Olesinski, R. W. & Abbaschian, G. J. The Ge-Sn (Germanium-Tin) system. *Bull. Alloy Phase Diagrams* **5**, 265–271 (1984).

28. Tran, T. T. *et al.* Ion beam synthesis and photoluminescence study of supersaturated fully-relaxed Ge-Sn alloys. *Mater. Sci. Eng. B Solid-State Mater. Adv. Technol.* **262**, (2020).

29. Ye, H. & Yu, J. Germanium epitaxy on silicon. *Sci. Technol. Adv. Mater.* **15**, (2014).

30. Liu, J., Sun, X., Camacho-Aguilera, R., Kimerling, L. C. & Michel, J. Ge-on-Si laser operating at room temperature. *Opt. Lett.* **35**, 679 (2010).

31. Reeber, R. R. & Wang, K. Thermal expansion and lattice parameters of group IV semiconductors. *Mater. Chem. Phys.* **46**, 259–264 (1996).

32. Roucka, R., Fang, Y. Y., Kouvetakis, J., Chizmeshya, A. V. G. & Menéndez, J. Thermal expansivity of Ge1-y sny alloys. *Phys. Rev. B - Condens. Matter Mater. Phys.* **81**, 1–6 (2010).

33. Holý, V., Pietsch, U. & Baumbach, T. *High-Resolution X-Ray Scattering from Thin Films and Multilayers*. (Springer, Berlin, Heidelberg, 1999). doi:https://doi.org/10.1007/BFb0109385

34. Kaganer, V., Köhler, R., Schmidbauer, M., Opitz, R. & Jenichen, B. X-ray diffraction peaks due to misfit dislocations in heteroepitaxial structures. *Phys. Rev. B - Condens. Matter Mater. Phys.* **55**, 1793–1810 (1997).

35. Frigerio, J. *et al.* Optical properties of highly n-doped germanium obtained by in situ doping and laser annealing. *J. Phys. D. Appl. Phys.* **50**, (2017).

36. Pastor, D. *et al.* High level active n + doping of strained germanium through co-implantation and nanosecond pulsed laser melting. *J. Appl. Phys.* **123**, (2018).

37. Sadofyev, Y. G., Martovitsky, V. P., Klekovkin, A. V., Saraikin, V. V. & Vasil'Evskii, I. S. Thermal stability of Ge/GeSn nanostructures grown by MBE on (001) Si/Ge virtual wafers. *Phys. Procedia* **72**, 411–418 (2015).

38. Xu, C., Senaratne, C. L., Culbertson, R. J., Kouvetakis, J. & Menendez, J. Deviations from Vegard's law in semiconductor thin films measured with X-ray diffraction and Rutherford backscattering: The Ge1-ySny and Ge1-xSix cases. *J. Appl. Phys.* **125702**, (2017).